JGR Atmospheres

RESEARCH ARTICLE
10.1029/2021JD035479

Special Section:
Southern Ocean clouds, aerosols, precipitation and radiation

Observations and Modeling of Rime Splintering in Southern Ocean Cumuli

Sonia Lasher-Trapp[1], Emma L. Scott[1,2], Emma Järvinen[3], Martin Schnaiter[3], Fritz Waitz[3], Paul J. DeMott[4], Christina S. McCluskey[4,5], and Thomas C. J. Hill[4]

[1]Department of Atmospheric Sciences, University of Illinois Urbana-Champaign, Urbana-Champaign, IL, USA, [2]Now at North Carolina Institute for Climate Studies, North Carolina State University, Asheville, NC, USA, [3]Karlsruhe Institute of Technology, Karlsruhe, Germany, [4]Department of Atmospheric Sciences, Colorado State University, Fort Collins, CO, USA, [5]Now at Climate and Global Dynamics Laboratory, National Center for Atmospheric Research, Boulder, CO, USA

Abstract Recent studies have suggested a correct representation of cloud phase in the Southern Ocean region is important in climate models for an accurate representation of the energy balance. Satellite retrievals indicate many of the clouds are predominantly liquid, despite their low temperatures. However, clouds containing high numbers of ice crystals have sometimes been observed in this region and implicated the secondary ice production process called rime splintering. This study re-examines rime splintering in Southern Ocean cumuli using both a new data set and high-resolution numerical modeling. Measurements acquired during the Southern Ocean Clouds Radiation Aerosol Transport Experimental Study (SOCRATES) provide an evaluation of the amount of ice in shallow cumuli sampled over two days in this region. The measurements sometimes exhibit seven orders of magnitude or more ice particles compared to amounts expected from measurements of ice-nucleating particles (INP) on the same days. Cumuli containing multiple updrafts had the greatest tendency to contain high ice concentrations and meet the expected conditions for rime splintering. Idealized numerical modeling, constrained by the observations, suggests that the multiple updrafts produce more frozen raindrops/graupel, and allow them to travel through the rime-splintering zone over an extended period of time, increasing the number of ice particles by many orders of magnitude. The extremely low number of INP in the Southern Ocean thus appears to require special conditions like multiple updrafts to help glaciate the cumuli in this region, potentially explaining the predominance of supercooled cumuli observed there.

Key Points:

- As much as seven orders of magnitude more ice was observed than expected from extrapolation of ice-nucleating particle measurements
- Clouds containing this ice had characteristics consistent with active rime splintering, and were more likely to have multiple updrafts
- Modeling suggests multiple updrafts allow time for the few ice-nucleating particles to produce larger ice needed for rime splintering

Supporting Information:

Supporting Information may be found in the online version of this article.

Correspondence to:

S. Lasher-Trapp,
slasher@illinois.edu

Citation:

Lasher-Trapp, S., Scott, E. L., Järvinen, E., Schnaiter, M., Waitz, F., DeMott, P. J., et al. (2021). Observations and modeling of rime splintering in Southern Ocean cumuli. *Journal of Geophysical Research: Atmospheres*, *126*, e2021JD035479. https://doi.org/10.1029/2021JD035479

Received 28 JUN 2021
Accepted 10 NOV 2021

1. Introduction

The Southern Ocean is a vast region largely isolated from anthropogenic pollution that contains prevalent low altitude clouds, effective at reflecting shortwave radiation compared to the otherwise absorptive ocean surface. Climate models have tended to underestimate the amount of reflected shortwave radiation in this region due to a lack of low cloud cover, particularly in the cold sectors of cyclones (Bodas-Salcedo et al., 2014, 2016; Naud et al., 2014; Vergara-Temprado et al., 2018). This lack of clouds likely results at least in part from difficulty in resolving the low-level meteorological features in the boundary layer as well as the inversion height (Williams et al., 2013). However, it might also result from model parameterizations glaciating these clouds too quickly (Kay et al., 2014; Vergara-Temprado et al., 2018). Cloud glaciation not only decreases its reflectivity to incoming solar radiation but also tends to increase precipitation amount and thus decrease cloud longevity, limiting the cloud lifetime (e.g., Pinto, 1998). Both effects might explain the high model bias in absorbed solar radiation over the Southern Ocean (Frey & Kay, 2018; Trenberth & Fasullo, 2010). Older satellite-based studies have suggested the prevalence of supercooled liquid water at cloud tops over the Southern Ocean (Hu et al., 2010; Huang et al., 2012), which would be more reflective than glaciated clouds, and could explain an underestimate in reflected shortwave radiation in climate models (e.g., Bodas-Salcedo et al., 2016; McCoy et al., 2014). Huang et al. (2012) also found that satellite retrievals of cloud optical depth were greater than climate models tend to predict.

The Southern Ocean Clouds Radiation Aerosol Transport Experimental Study (SOCRATES) was designed to gather in situ aircraft observations of aerosol and cloud properties in the Southern Ocean, in order to understand the influence of aerosol upon the cloud radiative properties, and to verify the accuracy of satellite retrieval products and numerical model predictions (McFarquhar et al., 2021). It was conducted in January and February of 2018; research flights with the NSF/NCAR G-V were based out of Hobart, Tasmania, and flew as far south as 62°S toward Antarctica. Aerosol and microphysical instrumentation, as well as radar and lidar systems, were

mounted on the aircraft. The majority of the flights were dedicated to sampling the large decks of stratocumulus prevalent in the cold sectors of cyclones. Two other flights conducted targeted sampling of shallow cumulus clouds. Studies based on the SOCRATES in-situ or remotely sensed aircraft data (e.g., D'Alessandro et al., 2021; Zaremba et al., 2020) support the results of past satellite retrievals that the majority (near 90%) of the summertime stratocumulus and cumulus cloud tops in this region are supercooled liquid. Mace et al. (2020) combined CloudSat radar and CALIPSO lidar data over the span of a year over the Southern Ocean and also found stratiform and shallow cumuliform clouds were predominantly supercooled liquid, and that the frequency of mixed-phase clouds appeared to increase with cloud/layer thickness and precipitation production.

The glaciation process must begin with the presence of some ice within the otherwise supercooled liquid cloud. The first ice is generated through primary nucleation, for which specific types of aerosol particles known as ice nucleating particles (INP) are required. INP can originate from a variety of sources, including mineral dust (e.g., Bunker et al., 2012), diverse biological entities (e.g., bacteria, fungi and pollen; see Huang, Siems, & Manton, 2021), and certain sea spray aerosols that may include biological particles and their organic matter exudates (DeMott et al., 2016; McCluskey et al., 2018; Saliba et al., 2021). For primary nucleation, a single ice particle results from each INP; the number of INP increases with decreasing temperature so more ice is nucleated in colder clouds. The number of INP is always far less, by orders of magnitude, than the number of cloud condensation nuclei (CCN). Over the Southern Ocean, INP number concentrations are extremely low (McCluskey et al., 2018), and primary ice production is likely insufficient to completely convert all the supercooled drops in a cloud to ice, especially in clouds warmer than −15°C (Blyth & Latham, 1997). Vergara-Temprado et al. (2018) conducted high-resolution regional numerical modeling over the Southern Ocean and associated the deficiency of INP with the maintenance of the supercooled liquid clouds. If and when enough ice exists, and if the supersaturation is low enough to evaporate droplets, the Wegener-Bergeron-Findeisen process could glaciate the clouds.

Secondary ice production (SIP) is the creation of additional frozen hydrometeors from a single ice particle without the aid of an INP (e.g., Field et al., 2017). These processes are hypothesized to explain frequently observed ice number concentrations that are orders of magnitude higher than measured or expected INP number concentrations. One of the most frequently studied SIP mechanisms is rime splintering (also known as the Hallet-Mossop process; Hallett & Mossop, 1974). Laboratory studies suggest that rime splintering requires supercooled droplets greater than 25 μm diameter riming onto the surface of a fast-falling frozen hydrometeor such as graupel or frozen raindrops, at an air temperature within −3 to −9°C. As the water inside the frozen outer shell of the collected supercooled droplet begins to freeze and expand, it exerts pressure (Choularton et al., 1978; Mossop, 1980) and shatters the icy perimeter of the drop, creating a spike of ejected water that then freezes. The spike splinters, ejecting fragments. Mossop (1976) found a splinter production rate of approximately one splinter per every 250 rimed drops. The rime splintering process can quickly increase ice number concentrations in the cloud, especially through the feedback of the ejected splinters growing (first by deposition but then by riming) into new graupel particles, or colliding with supercooled raindrops and freezing them, providing additional sites for rime splintering (Hallett et al., 1978).

Occurrences of high number concentrations of ice crystals coincident with the conditions for rime splintering have been documented around the world, including in the vicinity of the Southern Ocean. Mossop et al. (1970) observed ice number concentrations in glaciated small cumuli off the eastern and western coasts of Tasmania to be sometimes four orders of magnitude higher than predicted by the measured INP (10^{-2} L^{-1} at −15°C) from a ground site near the southeastern coast. Approximately half of the cumulus clouds sampled in the −5 to −10°C temperature range contained ice. They also noted that wider clouds (4–10 km) had a greater probability of containing ice, and hypothesized multiple updrafts (new turrets replacing older ones in the same cloud) were responsible for allowing the ice-forming conditions to be enhanced for a longer period of time, increasing the overall numbers of ice particles. More recently, Huang et al. (2017) and Huang, Hu, et al. (2021) reported aircraft measurements in shallow cumuli off the southwest coast of Tasmania that also appeared consistent with an active rime-splintering process. Although INP were not measured, ice number concentrations sometimes surpassed 50 L^{-1} when the cloud tops were warmer than −9°C. Aircraft data collected in predominantly supercooled stratiform clouds off the coast of Antarctica over the Weddell Sea by O'Shea et al. (2017) exhibited ice number concentrations exceeding 1 L^{-1} in small isolated regions that they attributed to rime splintering. Finlon et al. (2020) observed ice number concentrations sometimes exceeding 100 L^{-1} in a deep pre-frontal band of cloud associated with an atmospheric river extending south of Tasmania and implicated rime splintering as a likely source. In a region

of the world where satellite retrievals and recent in-situ aircraft studies suggest a predominance of supercooled liquid clouds, these studies documenting high ice number concentrations appear potentially difficult to reconcile: if large quantities of ice are possible in cumuliform clouds in this region due to rime splintering, what factor(s) would limit its production such that the clouds are still observed to consist predominantly of supercooled water?

Two flights during SOCRATES were dedicated to sampling summertime shallow cumuli in the Southern Ocean and presented an opportunity to revisit the topic of rime splintering there. These data were collected with more instrumentation than in past field studies, including aircraft measurements of the local INP over the ocean, a newer probe to measure small ice, and documentation of the cloud characteristics by a research radar on the aircraft. The flights of interest sampled fields of shallow cumuli as far as 53°S, 10 or more degrees farther south into the Southern Ocean than Mossop et al. (1970) or Huang et al. (2017) and Huang, Hu, et al. (2021), and are thus possibly less affected by any continental or anthropogenic aerosol sources to influence the INP. High-resolution numerical modeling is used to understand trends resulting from the observational analysis and possibly establish why cumuli may or may not produce abundant ice by rime splintering in the Southern Ocean.

2. Observations and Analysis

2.1. Overview of Data Collection and Macroscopic Cloud Characteristics

The sampling strategy for the two SOCRATES cumulus flights using the NSF/NCAR G-V aircraft consisted of first releasing dropsondes from 6 km altitude MSL to assess the environmental conditions en route to the cumulus field. These vertical profiles of temperature, humidity, pressure, wind speed, and wind direction were collected with the Airborne Vertical Atmospheric Profiling System (AVAPS; Hock & Franklin, 1999; Halverson et al., 2006). Afterward, the tops of active (growing) turrets were sampled within a few hundred meters of their tops as they ascended to the aircraft altitude. Constant altitude flight legs were performed within the environmental temperature range of −3 to −9°C, that is, the temperature zone in which rime splintering has occurred in laboratory studies. An additional pass sampled cloud bases, which sometimes included precipitation. Constant altitude clear-air legs were also flown above the cloud tops and below the bases to sample local aerosol particles, including INP. The clouds targeted for sampling were selected to represent the range of cumuli development present on each day, but deep cumuli were avoided. Multiple passes through the same turret were also avoided to prevent contamination of the measurements by aircraft-produced ice particles (APIPS; Rangno & Hobbs, 1983).

The NCAR High-performance Instrumented Airborne Platform for Environmental Research (HIAPER) Cloud Radar (HCR), a dual-polarization W-band radar (Vivekanandan et al., 2015), was used to document the cloud structure at the time of sampling. The unidirectional radar pointed downward from the aircraft flight level, except when sampling at or beneath the cloud bases. The along-beam resolution of the data was 30–50 m for the altitudes used during the cumulus sampling. Due to the short beam wavelength, attenuation can occur in even moderate precipitation. The vertical orientation necessarily includes cloud particle fall speeds superimposed upon updrafts and downdrafts and thus does not reliably indicate maximum updraft and downdraft strengths in the cloud. As a result, the radar data are mainly used here to document the macroscopic cloud structure and stage of cloud development during sampling, including the discrimination of clouds with single or multiple updrafts based on observed radial velocity. Radar data are only available from the aircraft, so the time history of a particular cloud is unknown.

The first field of cumulus was sampled on 17 February 2018 (Figure 1a). The dropsonde released immediately before cumulus sampling at 030258 UTC (Figure 1a, southernmost circle, data plotted in Figure S1a in Supporting Information S1) showed a well-mixed boundary layer with a lifting condensation level near 900 hPa (0°C) and an equilibrium level near 700 hPa (−12°C). Wind shear was negligible over this depth. The cloud base height was approximately 1000 m MSL, and the highest cloud sampling altitude was 2200 m MSL. Aerosol sampling in the clear air was conducted below the bases at 150 m MSL and above cloud tops at 4500 m MSL. Clouds on this day often contained multiple updrafts (Figure 2a) and tended to be 3000–4000 m wide and 1500 m deep. Images from the Particle Habit Imaging and Polar Scattering (PHIPS) probe (Figure 3a) included liquid drops, heavily rimed ice, and graupel/rimed frozen raindrops.

A second shallower field of cumulus was sampled on 24 February 2018 (Figure 1b). Here too, the dropsonde released immediately before sampling (Figure S1b in Supporting Information S1) showed a boundary layer with a lifting condensation level near 900 hPa (0°C), but a strong inversion immediately below 800 hPa (−4°C) limited

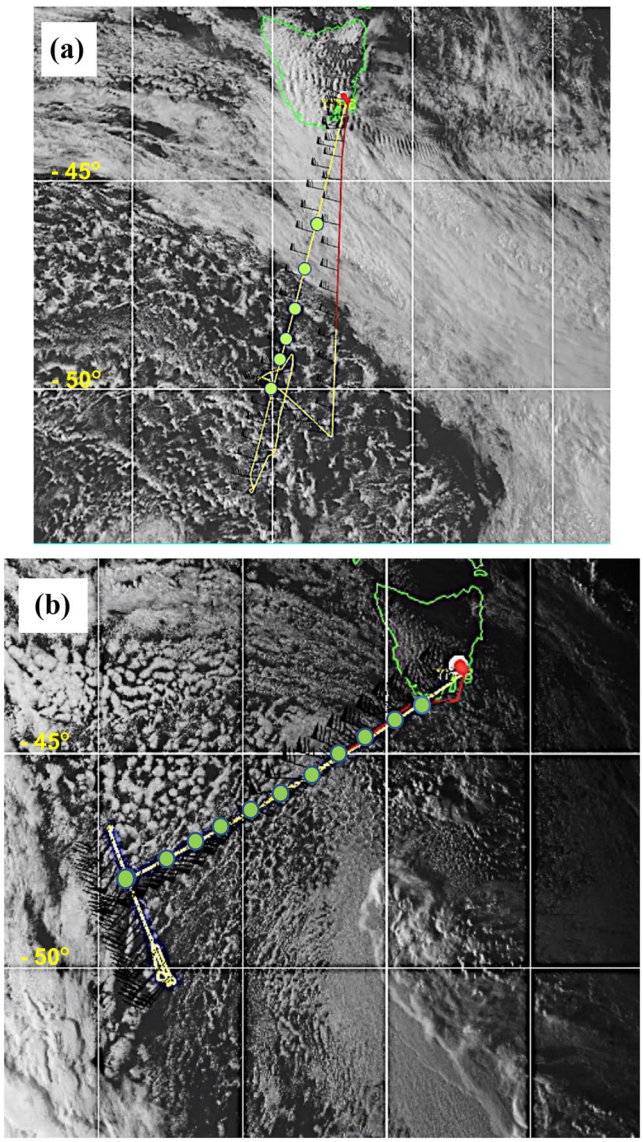

Figure 1. G-V flight path with dropsonde locations (green dots) and wind barbs plotted, overlaid upon Himawari visible satellite data, for (a) 17 February 2018 and (b) 24 February 2018. Cumulus sampling was conducted after the last dropsonde was released.

the maximum cloud top heights. Wind shear was again very weak over the cloud layer. The sampled cloud bases were at 1,000 m altitude MSL, but the maximum cloud sampling altitude was only 1,500 m. Aerosol measurements in the clear air were collected below the bases at 170 m MSL, and above the tops at 2,200 m MSL. The clouds on this day often contained only single updrafts (Figure 2b) and were typically only 1,000 m in width and depth. For most of these clouds, the PHIPS probe captured images of liquid drops, but some ice with little riming was evident for one cloud pass (Figure 3b).

2.2. Measurements and Data Processing

The NSF/NCAR G-V aircraft carried a variety of microphysical instrumentation; a full description is given by McFarquhar et al. (2021). The microphysical data used in this study include: size distributions of cloud droplets from 2 to 50 μm diameter from the Cloud Droplet Probe (CDP; Lance et al., 2010), the presence of supercooled cloud droplets as indicated by the Rosemount Icing Detector (RICE; Baumgardner & Rodi, 1989), the presence of graupel/rimed frozen raindrops as indicated by 2D images of particles 200–1,600 μm in diameter (with 25 μm resolution) from the 2DC Probe (for which occasional condensation on the probe mirrors during SOCRATES made number concentrations unreliable Finlon et al., 2020), and liquid and ice particle size distributions and images for particles 60–700 μm and 20–700 μm in diameter (with 6.2–6.8 μm resolution, depending on the camera taking the images), respectively, from the PHIPS probe (Abdelmonem et al., 2016; Schnaiter et al., 2018; Waitz et al., 2021). Phase discrimination by the PHIPS probe is based on analyzing the shape of the single particle angular scattering function as described in detail by Waitz et al. (2021) where it was shown to be 98% accurate. The scattering function is only weakly dependent upon particle size, so phase discrimination could be conducted down to the minimum detectable ice particle size, which was set to 20 μm for SOCRATES. A 2DS probe (Lawson et al., 2006) was also flown on the aircraft but its use was limited here because data were not recorded for one of the two flights (24 Feb flight). Measurements of INP, acting in the immersion freezing mode, were determined from the total particles collected with a filter system drawing from a HIAPER modular inlet (HIMIL), and later suspended and quantified in the laboratory. INP collection and processing methods are described in detail by Levin et al. (2019), and protocols specific to the SOCRATES data set are discussed in Supporting Information S1.

Ice particles can sometimes collide with probes and shatter, artificially inflating number concentrations and decreasing mean sizes (e.g., Korolev et al., 2011), and this can also occur with the PHIPS probe. In the standard release of the PHIPS data set, the data are automatically flagged as possibly influenced by shattering when more than 10% of all particles measured by the 2DS at that time exceed 800 μm diameter (Waitz et al., 2021). However, in this study, the presence of such large particles on the optical array probes is often indicative of graupel/frozen raindrops, which are a necessary ingredient for the rime-splintering process, so additional manual scrutiny of the PHIPS data for all 32 of the cloud passes was performed to attain careful, best estimates of the number concentrations of ice particles less than 60 μm diameter. The analysis (explained in detail in Supporting Information S1) included (a) manual identification of "satellite" ice particles or individual particles that looked like shattering fragments in the stereo-images, (b) agreement among the PHIPS and 2DS particle size distributions (17 Feb flight only), and (c) frequency of the automated shattering flag during the period. Based on these three factors, the degree of confidence in the shattering assessment for each cloud pass was assigned integer values: −2 for shattering with high confidence; −1 for shattering with low confidence; +1 for no shattering with medium confidence; or +2 for no shattering with high confidence, as listed in Tables S1–S3 in Supporting Information S2. For cloud passes flagged with a value of −2 or −1, the one-second samples

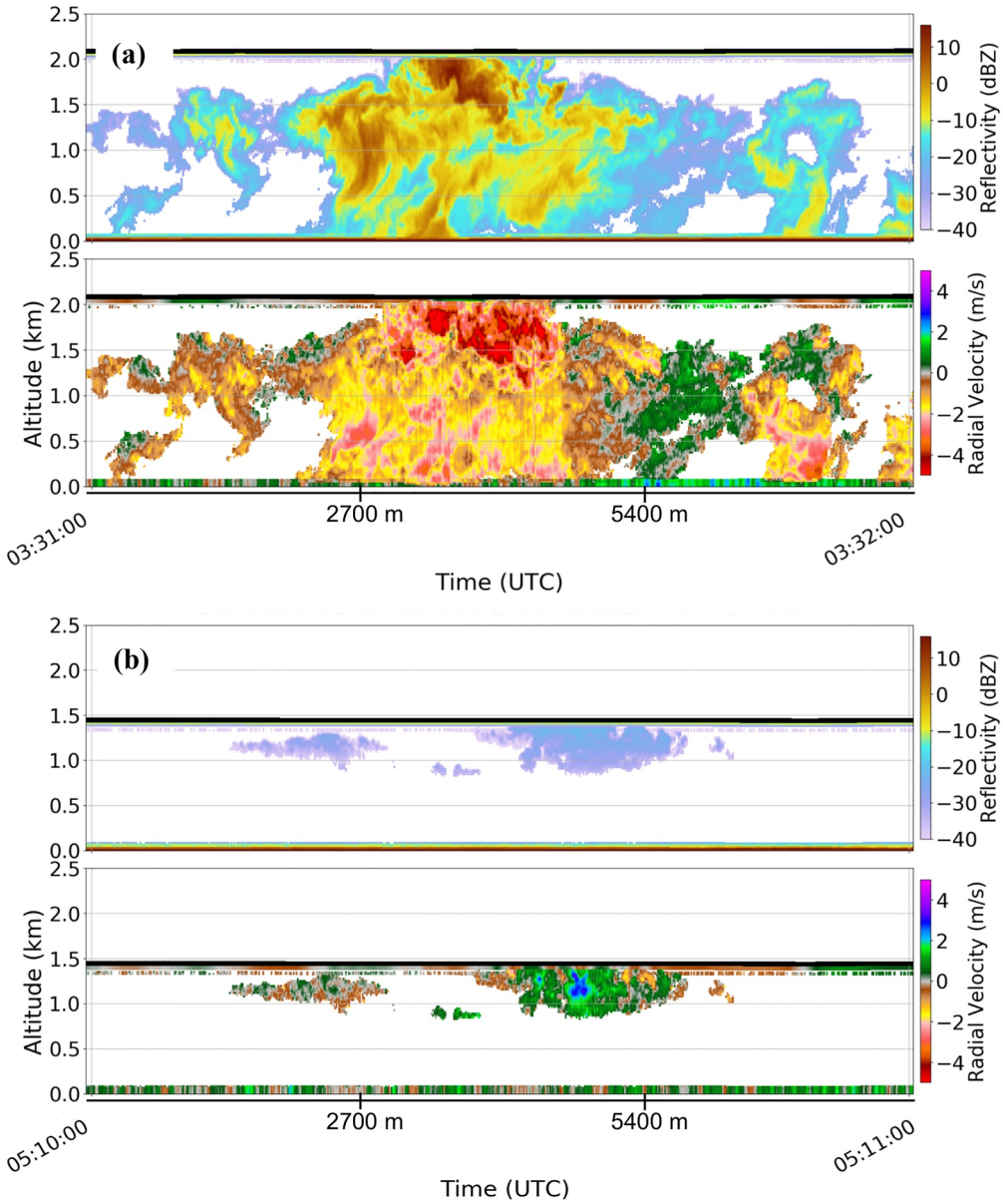

Figure 2. Cloud passes showing HCR reflectivity (top panels) and relative velocity (bottom panels) with time, distance, and color scales as indicated, for (a) 033120 UTC on 17 February 2018 and (b) 051030 UTC on 24 Feb 2018. HCR pointed downward from the aircraft, so cloud top heights not visible.

suggestive of shattering were not used in the average ice number concentrations, but these averages should still be viewed with less confidence, and are not used in the plots shown later. If all seconds were flagged in the cloud pass, the ice number concentration for the entire cloud pass was not quantified (dashed entries in Tables S1–S3 in Supporting Information S2).

2.3. Analysis of Primary Ice Nucleation and Rime Splintering

Immersion-freezing INP number concentrations from the below-cloud base sampling from these two cumulus flights (Figure 4) fall in the lower range of values that typify other remote oceanic regions (DeMott et al., 2016; McCluskey et al., 2018) but follow similar trends of exponentially decreasing values with increasing temperature. On both days, immersion-freezing INP sampled near 150 m above the ocean surface were sufficiently low that collected volumes did not exhibit freezing at temperatures greater than −18°C. In general, more INP were

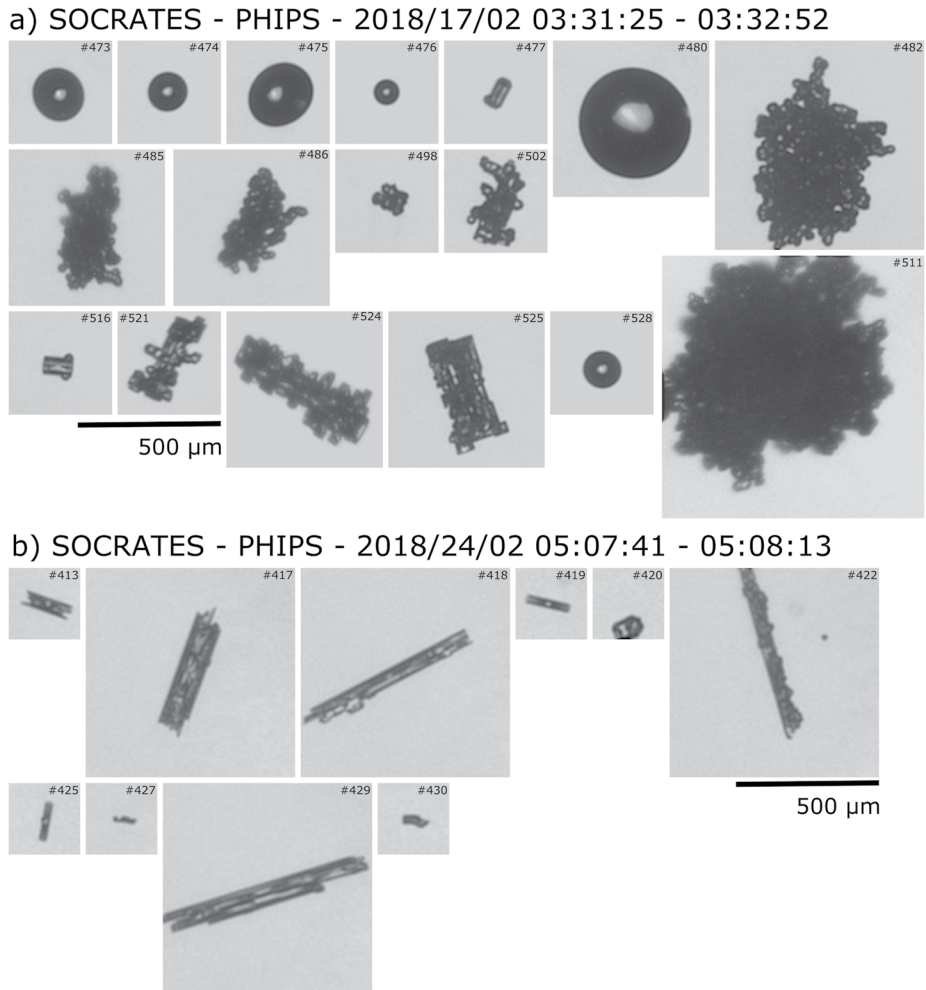

Figure 3. Examples of particle images from the PHIPS probe for (a) 17 February 2018 and (b) 24 February 2018. Reference scale bars in both panels represents a length of 500 µm.

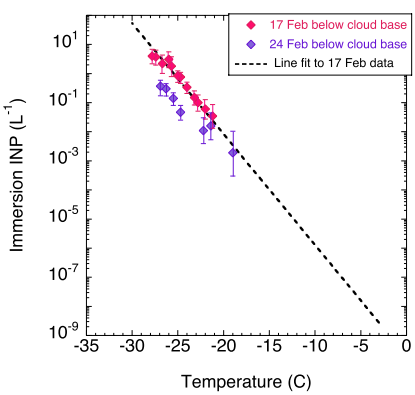

Figure 4. Analyzed filter measurements of immersion-freezing INP versus temperature, with 95% confidence intervals denoted by vertical lines, collected below the cloud bases on dates shown. Line fit to the 17 Feb data, extrapolated to higher temperatures, is used in the numerical modeling.

observed on 17 Feb than on 24 Feb. A line fit to the 17 Feb measurements, extrapolated to temperatures at which the cloud sampling was conducted, implies that primary nucleation of ice by immersion-freezing could only produce a maximum of 10^{-7} L^{-1} ice crystals in the rime-splintering temperature zone (−3 to −9°C). It is unknown of course if the simple log-linear extrapolation adequately captures the low end of INP concentrations active at the higher unsampled temperatures. Vignon et al. (2021) showed that immersion freezing INP measurements collected with filters exposed for 24–48 hr from a ship platform located near the Mawson Antarctic coastal station suggest a log-linear extrapolation with a different slope in the temperature regime of interest here, resulting in 10^{-5} L^{-1} as an upper bound for INP concentrations within the rime-splintering temperature zone. Spectra of INP from filters exposed for 24 hr aboard the RV Tangaroa at 50–80°S, which had limits of detection near −15°C (Kremser et al., 2021), suggest an INP concentration of 10^{-5} L^{-1} at −13°C, matching the concentrations predicted in the extrapolation in Figure 4. Regardless, all these estimates suggest that the observed ice should have very low number concentrations if primary nucleation alone is active. Otherwise, INP concentrations would have been observable within the limits of detection.

Because rime splintering cannot be directly witnessed in the observational data, it must be inferred from the "necessary conditions" for its operation based upon laboratory studies:

1. Cloud top within or above altitudes having temperatures in the range of −3 to −9°C.
2. The presence of supercooled cloud droplets for riming, including some greater than 25 μm diameter.
3. The presence of rimed particles, including graupel/frozen raindrops.
4. As a result, small ice particles in number concentrations exceeding the measured INP.

The measured in-cloud temperature was used to determine if a cloud pass met condition (1). For condition (2), the RICE probe was first used to determine regions with supercooled liquid droplets, and within those regions, the number of CDP-detected particles exceeding 25 μm diameter as measured by the CDP were noted (detection limit approximately 0.003 cm^{-3} over the ten-second period used). Large rimed particles (including graupel/rimed frozen raindrops) were identified manually in the 2DC (as in Lasher-Trapp et al., 2016) or PHIPS images as any non-spherical particle 200 μm or larger in diameter where the original crystal habit was indistinguishable due to the buildup of rime (2DC detection limit approximately 0.02 L^{-1}). For condition (4), small ice particles were defined as PHIPS-measured ice 20–60 μm diameter, and given the small sample volume for these sizes of particles (approximately 27 $cm^{-3}s^{-1}$ at a flight speed of 150 m s^{-1}) yields a minimum detection limit of 3.8 L^{-1} over a 10-s period. This detection limit is well above the observed INP in the −3 to −9°C temperature range, so some cloud passes where small ice was not detected might still have been experiencing rime splintering.

If all conditions (1–4) were met, the cloud pass was categorized as *likely* having rime splintering. Other cases lacked small ice, or were flagged for possible shattering, and were thus labeled as *possibly* having rime splintering. Cases sampled in the rime splintering temperature zone that lacked two or more criteria were labeled as *unlikely* to have rime splintering, including if no ice was detected by the PHIPS probe. However, some of these *unlikely* cases might still have contained much more ice than the observed INP but in amounts less than detectable by the PHIPS probe. The number of *unlikely* cases may be inflated as a result.

2.4. Classification of the Sampled Clouds

Tables S1–S3 in Supporting Information S2 summarize the conditions of the *likely*, *possibly*, and *unlikely* rime splintering cloud passes, respectively, as explained further in Supporting Information S1. A cloud pass in the aircraft data was defined as a constant-altitude, continuous region of non-zero radar echo up to 10 s long. If the cloud pass was longer than 10 s, the 10-s interval of the strongest radar echo was used. If a cloud pass was flagged with a −1 or −2 value for shattering, it was retained in Tables S1–S3 in Supporting Information S2 but not used in the plots shown later in this section.

Of the 32 total cloud passes analyzed, eleven (34%) met all the criteria and thus were designated as *likely* having rime splintering. All occurred on 17 February, and average total PHIPS ice number concentrations sometimes reached several hundred per liter. An additional three cloud passes (9%) met most of the criteria, but either lacked ice quantification due to the detection limit of the PHIPS probe or suspected contamination by shattering effects as described in Supporting Information S1. These three cases were deemed *possibly* having rime splintering. The remaining 18 cloud passes (56%) lacked several criteria for rime splintering; most lacked any detection of ice by the PHIPS probe and thus were considered *unlikely* to have rime splintering occurring. Some of these passes occurred on 17 February, but the majority of clouds sampled on 24 Feb fell into this category. Across all the cloud passes, 38% had no ice detected at all by the PHIPS probe nor any graupel/frozen raindrops in the 2DC images.

The amount of ice detected by the PHIPS probe for each cloud pass coincides well with their categorization of the likelihood of rime splintering (Figure 5a). Even after consideration of shattering effects, PHIPS average total ice concentrations (for all ice less than 700 μm diameter) were quite large, once exceeding 300 L^{-1} (minimum detection limit for 700 μm particles of 0.75 L^{-1} over a ten-second cloud pass), while the maximum amount of immersion-freezing INP expected at (i.e., extrapolated to) the lowest sampling temperatures would have only been on the order of 10^{-7} L^{-1}. Because the sampling was performed near the cloud tops, the data shown at lower temperatures in Figure 5a were collected in deeper clouds (passes at temperatures less than −5°C only occurring for the 17 Feb flight), and those shown at higher temperatures were collected in shallower clouds (during both flights). No clear relationship emerges between cloud depth and the maximum ice observed.

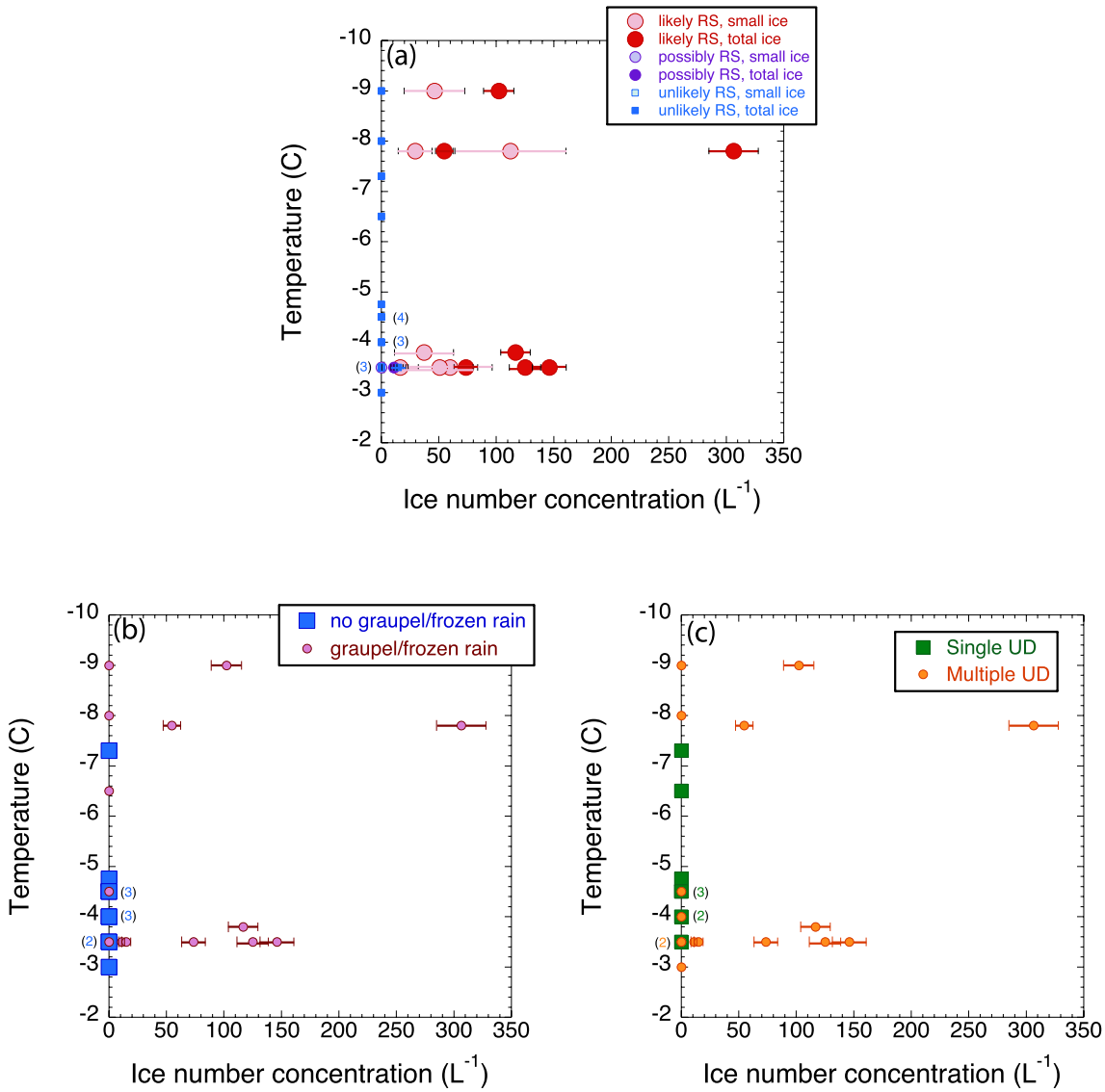

Figure 5. (a) Averages of PHIPS number concentration of "small ice" ($D < 60$ μm) or "total ice" ($D < 700$ μm) versus sampling temperature for the cloud passes listed in bold in Tables S1–S3 in Supporting Information S2. Symbols color-coded based upon their classification as "likely," "possibly," or "unlikely" having rime splintering as discussed in the text, with uncertainties based on the number of detected particles; (b) As in (a) but only "total ice" plotted for cases with or without graupel/rimed frozen raindrop images in the 2DC data; (c) As in (b) but plotted for cases having single or multiple updrafts (UD) in the cloud as seen on the HCR or aircraft gust pod. For all panels (a)–(c), numbers in parentheses denote number of cloud passes (if greater than one) at that temperature having no ice recorded by the PHIPS probe.

Although the detection of large irregular images on the 2DC (assumed graupel or rimed frozen raindrops) was a necessary condition for any cloud pass to be considered as *likely* having rime splintering, independent of the assigned likelihood, their detection during a cloud pass was a good predictor of higher observed ice number concentrations (Figure 5b). These large frozen particles, in turn, should correspond to high updraft speeds (needed to suspend heavier ice particles in the cloud; at least several meters per second, e.g., Bohm, 1989) and high amounts of supercooled liquid water in the clouds. However, because the aircraft predominantly sampled very near the cloud tops (to try to sample the smallest ice particles, which would be suspended higher in the cloud), the aircraft-measured updraft speeds listed in Tables S1–S3 in Supporting Information S2 are not representative of the maximum in the cloud, nor would the aircraft have encountered the maximum liquid water content. (The radar-sensed vertical velocities necessarily contain the effects of the larger hydrometeor fall speeds, so are also not indicative of the maximum updraft speeds.)

However, the presence of multiple updrafts, ascertained by the radar and aircraft data, was also very indicative of high ice number concentrations in the clouds (Figure 5c). Multiple updrafts can supply additional liquid water content for riming (e.g., Blyth & Latham, 1993, 1997; Moser & Lasher-Trapp, 2017), and perhaps additional time (Mossop et al., 1970) for riming growth of the graupel or frozen raindrops, ultimately producing more rime-splinters. The multiple updraft clouds also consistently contained evidence of these large frozen hydrometeors (comparing Figures 5b and 5c).

These (albeit, limited) observations suggest that if clouds lack a multiple updraft structure, graupel/frozen raindrops and high ice number concentrations are less likely, and perhaps it is this aspect that allows the prevalence of supercooled cumuli in this region. In the next section, this hypothesis is further investigated with 3D high-resolution, idealized numerical modeling of the cumuli, uniquely using the amount of observed INP as a basis for primary ice nucleation.

3. Numerical Modeling

3.1. Model and Setup

Cloud Model 1 (CM1; Bryan & Fritsch, 2002) is a three-dimensional, non-hydrostatic model that evaluates equations governing the three Cartesian velocity components, pressure, potential temperature, and mixing ratios of water vapor and hydrometeors; this study used CM1 version 19.6. The domain was 11 km wide in both horizontal directions, and 4.1 km deep with a constant grid spacing of 25 m. The model environmental state was initialized with the dropsonde data released in the cumulus region immediately before the start of cumulus sampling on 17 February (Figure S1a in Supporting Information S1). Winds from this profile were excluded from the modeling setup due to their high speeds which would require much larger computational domains. The vertical wind shear over the heights of interest (up to 4 km, ~650 mb) was minimal and thus excluding the winds does not affect the realism of the simulated cloud structure.

A new cloud forcing scheme was added to CM1 for this study to initiate cumulus updrafts without any heat perturbation (unlikely to occur over the well-mixed ocean surface). This initiation scheme (shared by J. Straka, personal communication, 2013) adds an enhanced vertical acceleration within a prescribed sphere. The resulting area of ascent produces the initial cloud updraft. The time-dependent forcing consists of periods during which the vertical acceleration is linearly increased, then sustained, and then relaxed to zero. The forcing is maximized at the center of the sphere and decreases toward its edge according to a squared cosine function. Multiple spheres of vertical acceleration can be user-specified to produce multiple updrafts at different locations, strengths, and times (Table 1).

The double-moment NSSL scheme (Mansell et al., 2010) was used here, with some modifications. For this study, ice categories included small ice (mean diameter less than 100 μm), snow (that includes aggregates as well as individual ice crystals with mean diameter greater than 100 μm, and tiny frozen cloud droplets too small to be classified as graupel), and " graupel" that also includes frozen raindrops. The NSSL scheme explicitly predicts supersaturation for droplet nucleation, based on a user-input value of CCN for an activity spectrum (Cs^k, where C and k are constants and s is the supersaturation), and C was set to 150 cm^{-3} to recreate the observed number concentration of cloud droplets at the bases. For this study, *all options of primary nucleation of ice were disabled* (including the default contact nucleation scheme Meyers et al., 1992 and the default immersion freezing scheme Bigg, 1953). Instead, a new immersion-freezing scheme, designed specifically for the shallow Southern Ocean cumuli and based on the observed immersion-freezing INP for 17 February, was used to estimate the primary nucleated ice that could possibly initiate rime splintering.

The new algorithm calculates the number of immersion-freezing INP that would be distributed over the population of cloud droplets if they were contained within some of the particles acting as CCN. The possible amount of INP contained within raindrops is also considered by assessing the average number of cloud droplets contained within a raindrop. The algorithm uses the following equations within cloudy grid boxes where the vertical velocity exceeds 0.1 m s^{-1} (i.e., cloudy air cooling as it ascends) to freeze a number of cloud droplets in the grid box (N_{cfrz}) and a number of raindrops in the grid box (N_{Rfrz}):

Table 1
Cloud Forcing for Single or Multiple Updraft Simulations

Updraft forcing	"Single updraft- weak"	"Single updraft- strong" (RS on or off)	"Multiple updrafts" (RS on or off; 10^3 fewer or more INP)
Forcing width, depth	1,000 m width and 200 m depth		
Height of center of forcing	800 m height		
Forcing time evolution	300 s linear increase, 300 s full strength, 300 s linear decrease		
Updraft 1			
Max vertical accel. (m s^{-2})	0.5	1.0	1.5
Center location (*x*,*y*; km)	(4.8,4.8)	(4.8,4.8)	(4.8,4.8)
Initiation time (s)	0	0	0
Updraft 2			
Max vertical accel. (m s^{-2})			2.0
Center location (*x*,*y*; km)	–	–	(5,5)
Initiation time (s)			600
Updraft 3			
Max vertical accel. (m s^{-2})			2.0
Center location (*x*,*y*; km)	–	–	(5,5)
Initiation time (s)			1200
Updraft 4			
Max Vertical Accel. (m s^{-2})			2.5
Center location (*x*,*y*; km)	–	–	(5,5)
Initiation time (s)			1800
Updraft 5			
Max vertical accel. (m s^{-2})			1.5
Center location (*x*,*y*; km)	–	–	(5,5)
Initiation time (s)			2400
Updraft 6[a]			
Max vertical accel. (m s^{-2})			2.5
Center location (*x*,*y*; km)	–	–	(5,5)
Initiation time (s)			3000
Updraft 7			
Max vertical accel. (m s^{-2})			1.0
Center location (*x*,*y*; km)	–	–	(5,5)
Initiation time (s)			3600
Updraft 8			
Max vertical accel. (m s^{-2})			0.5
Center location (*x*,*y*; km)	–	–	(5,5)
Initiation time (s)			4200

[a]Forcing had a linear increase for 500 s, full strength for 300 s, and no linear decrease.

$$N_{cfrz}(T) = \left[\frac{N_{\text{inp}}(T)}{N_{\text{co}}} N_{\text{ctot}} - N_{\text{ice}}\right](\alpha - 1) \tag{1}$$

$$N_{Rfrz}(T) = \left[\frac{N_{\text{inp}}(T)}{N_{\text{co}}} N_{\text{ctot}} - N_{\text{ice}}\right]\alpha \tag{2}$$

where $N_{\text{inp}}(T)$ is the number of INP active at temperature T as given by the curve fit to the 17 Feb SOCRATES INP data (Figure 4) and extrapolated to temperatures up to −3°C:

$$N_{inp} = N_0 \exp\left[\beta(-T)\right] \tag{3}$$

with $N_0 = 2 \times 10^{-7}$ m^{-3} and $\beta = 0.8776$. In Equations 1 and 2, N_{co} is the average number of cloud droplets nucleated near cloud base (150 cm^{-3}), N_{ice} is the number of ice hydrometeors in the grid box (a rough estimate of the INP already nucleated at higher temperatures, including any ice, snow and graupel, so as to only nucleate ice for the new amount of cooling), N_{ctot} is the total number of cloud droplets in the grid box (including an estimate of the number contained within a raindrop by dividing the average raindrop volume V_R by the average cloud droplet volume V_c) and α is the fraction of N_{ctot} that makes up the raindrops:

$$N_{\text{ctot}} = N_c + \frac{V_R}{V_c} N_R \tag{4}$$

$$\alpha = \frac{\frac{V_R}{V_c} N_R}{N_{\text{ctot}}} \tag{5}$$

where N_c is the number of cloud droplets in the grid box and N_R is the number of raindrops in the grid box. This immersion-freezing algorithm is dependent on temperature alone (time-dependence is ignored) and operates at temperatures less than −3°C.

The default rime-splintering algorithm in the NSSL scheme was retained. It is the second formulation of Cotton et al. (1986), where 1 splinter is created per 250 drops accreted onto a rimed particle within the −3 to −9°C temperature range. Supercooled raindrops can also collect cloud ice (that includes rime-splinters) to produce graupel; they do so with a collection efficiency of 0.5, an intermediate value from the range found in the laboratory by Lew and Pruppacher (1983). Once any secondary ice is produced by rime-splintering, N_{ice} will always exceed N_{inp} from the INP formula, and thus, no new ice will be nucleated by immersion-freezing. This omission of newly nucleated primary ice is very small relative to the numbers of ice crystals produced by rime splintering, but given the possible feedback into producing more graupel and thus rime splintering, the amounts of ice produced in the model should be considered lower estimates.

3.2. Simulation Results

The observational analysis in Section 2 suggested that cumuli consisting of a single updraft were less likely to contain evidence of rime splintering than those having multiple updrafts. Two sets of cloud simulations were performed, each including or disabling rime splintering, with one set having a single updraft (simulations run for 1800 s) and the other set having multiple updrafts (simulations run for 6000 s).

3.2.1. Single Thermal

In the first set of simulations, a single updraft was initiated with either weaker or stronger forcing (Table 1). In these cases, the cloud formed about 5 min into the simulation, reached its maximum cloud top height approximately 10–13 min later, and had mostly disappeared by 25 min from its start (Figures 6a and 6e). The 75th/90th percentile updraft speeds (not shown) were near 5/6 and 7/9 m s^{-1}, for the weaker and stronger forcing respectively, but decreased near the cloud tops to maxima consistent with the 1–4 m s^{-1} that the aircraft had sampled near the cloud tops. The simulated cloud bases were near 1000 m (Figures 6a and 6e), in accord with the observations. The weaker forcing produced a cloud top at 2.2 km and −9°C (Figure 6a), coinciding with the lowest

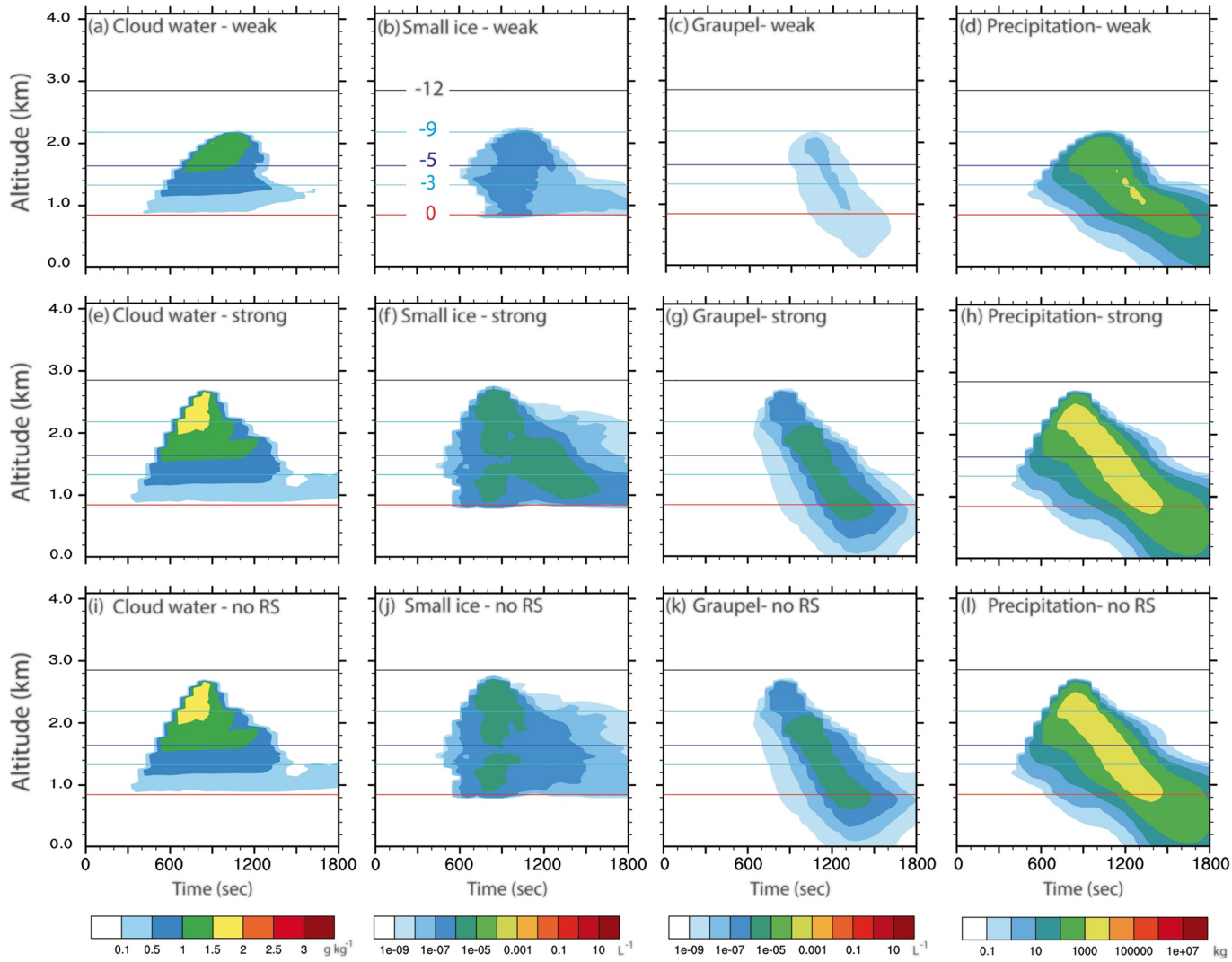

Figure 6. Time-height diagrams for the single updraft simulations with weaker forcing ("weak"; top row), stronger forcing ("strong"; middle row), and same stronger forcing but with rime splintering turned off ("no RS"; bottom row). Panels show: (a), (e), and (i) Maximum cloud water mixing ratio; (b), (f), and (j) Maximum small ice number concentration; (c), (g), and (k) Maximum graupel (including frozen raindrops) number concentration; (d), (h), and (l) Total precipitation (rain, snow, and graupel) mass, shaded according to color bars at the bottom of each column. Horizontal lines labeled in (b) show environmental isotherms in °C for all panels.

temperatures sampled (Figure 5), while the stronger forcing produced a higher cloud top at 2.75 km and −11°C (Figure 6e). An additional stronger-forced simulation was also performed with rime-splintering disabled (Figures 6i–6l).

The cloud with the lower (and thus warmer) top due to the weaker forcing nucleated minimal amounts of small ice (maximum of 10^{-7} L^{-1}; Figure 6b) from the immersion-freezing scheme based on the SOCRATES INP measurements, whereas the cloud with the higher (and cooler) cloud top produced an order of magnitude more (Figure 6f). The strong updraft and greater amount of cloud water (Figure 6e) favored an earlier production of precipitation (Figures 6d and 6h) that consisted primarily of raindrops. Some of those raindrops froze from the SOCRATES immersion-freezing INP to produce the first "graupel" in the model about 5 min earlier in the stronger cloud (Figures 6c and 6g); immersion freezing of cloud drops also made snow a few minutes earlier (not shown). As the graupel fell through the rime-splintering zone in the deeper cloud, it initiated rime splintering approximately 900 s into the simulation (comparing Figures 6f and 6j). The production of rain, graupel, and rime-splinters continued to add to the maximum ice number concentrations in the deeper cloud, reaching 10^{-6} L^{-1} (adding panels 6f and 6g). Similar magnitudes of ice were attained in the absence of rime splintering but persisted for a shorter time (Figure 6j). In contrast, the smaller amount of cloud water in the weaker cloud (Figure 6a) slowed its rain

production, and although some graupel was produced by the immersion-freezing of some raindrops, they were insufficient to initiate any appreciable rime splintering as the cloud was collapsing (Figures 6a–6c).

These simulations thus support several tendencies found in the observational analysis. They both generated maximum small-ice number concentrations well below the PHIPS probe detection limit (approximately 4 L^{-1} for ice less than 60 μm diameter); the model suggests the single-updraft clouds observed were unable to make sufficient amounts of graupel/frozen raindrops to initiate much rime splintering within their short lifetimes. The modeling also suggests that a single updraft in a slightly deeper cloud than observed during the two SOCRATES flights could produce more graupel/frozen raindrops to initiate rime-splintering as a result of not only increased primary ice nucleation from the colder cloud top but also the increased cloud water that produces raindrops more quickly, that then can freeze by immersion to generate the first large riming particles, earlier in the cloud lifetime. Nonetheless, the model also suggests that even a slightly deeper, single updraft cloud would be unlikely to produce the 10 to 100 L^{-1} ice number concentrations observed. Even though some rime-splintering was active, it had negligible effects upon precipitation formation in these single-updraft clouds (comparing Figures 6h and 6l).

3.2.2. Multiple Thermals

It was hypothesized from the observational analysis that multiple updrafts within a cloud might provide more cloud water for graupel (and frozen raindrop) production, which are major drivers of the rime-splintering process, and extend the time that they can be created and traveling through the rime-splintering zone, increasing the numbers of ice created by rime splintering. Simulations with a series of eight successive updrafts (Table 1) produced ice number concentrations within the range of maxima observed during the 17 Feb case (over 10 L^{-1}; Figure 7c). [Presumably different combinations could be found for the forcing characteristics that could attain the same amount of ice with fewer, or require more, updrafts. The use of eight updrafts here is not meant to indicate this is a general number needed.] The increasingly stronger forcing of the first four updrafts was found to be necessary to prevent "destructive interference" between the previous turret's collapse and the updraft of the new turret, leading to 75th/90th percentiles of updraft speeds of 5/10 m s^{-1}, with values close to the aircraft-measured values near cloud top. The cloud top pulsed up to 3.2 km at times, attaining temperatures less than −12°C, but within the range suggested by satellite estimates at this time in the sampling region for the 17 Feb case (Figure S2 in Supporting Information S1). The overall simulated cloud lifetime exceeds 80 min but does not seem unreasonable for a multi-turret cloud, although the lack of continuous radar data on any particular cloud prevents a formal assessment of its realism.

The first updraft/turret of this simulation (lasting up to about 1000 s) was about 500 m deeper than the stronger single-updraft case, and thus also contained about 0.5 g kg^{-1} more cloud water (Figures 6e and 7a). It thus attained an order of magnitude more small ice by immersion-freezing (Figures 6f and 7c). Graupel/frozen raindrop number concentrations in the first turret were similar to those of the stronger single updraft case, but extended higher into the cloud (Figures 6g and 7e). The amount of small ice in the cloud was only 10^{-4} L^{-1} at this time (Figure 7c).

A comparison of the multi-updraft simulation with rime splintering permitted and disabled shows the significance of multiple cloud updrafts/turrets in enhancing ice production by rime splintering. After the first updraft/turret reached its peak height (near 700 s), its collapse carried ice downward with it, but some was again lifted by the second stronger updraft into regions of higher cloud water where riming was enhanced. At the time of the collapse of the second updraft (~1400 s), the descent of graupel (including frozen raindrops) through the rime-splintering zone contributed to additional small ice (Figures 7c and 7d near −5°C level). Subsequent updrafts followed a similar scenario, replenishing cloud water (Figure 7a) for enhanced riming within the rime-splintering zone, such that an order of magnitude more small ice became apparent in the rime-splintering zone after 2200 s (Figures 7c and 7d), and continued to increase at those altitudes (and above, as the rime-splinters were carried aloft in new updrafts). In time (by 3200 s), this extra ice fed back into the freezing of more supercooled raindrops by collection (Figures 7e and 7f), that further enhanced rime splintering. In both simulations, the liquid rain mass dominated the graupel mass (not shown) by several orders of magnitude until 4200 s, after which time the graupel and rain masses were comparable, and the simulated cloud even produced a strong shower of graupel at the ocean surface (Figure 7e). [In the simulation without rime splintering, the graupel mass was quite limited (Figure 7f)]. The collapse of the seventh updraft (near 4600 s) yielded the simulation-maximum small ice number concentration (Figure 7c; exceeding 20 L^{-1}), five orders of magnitude higher than without rime splintering (Figure 7d), and in accord with some of the observed maxima on 17 Feb found in clouds with multiple updrafts. Although rime

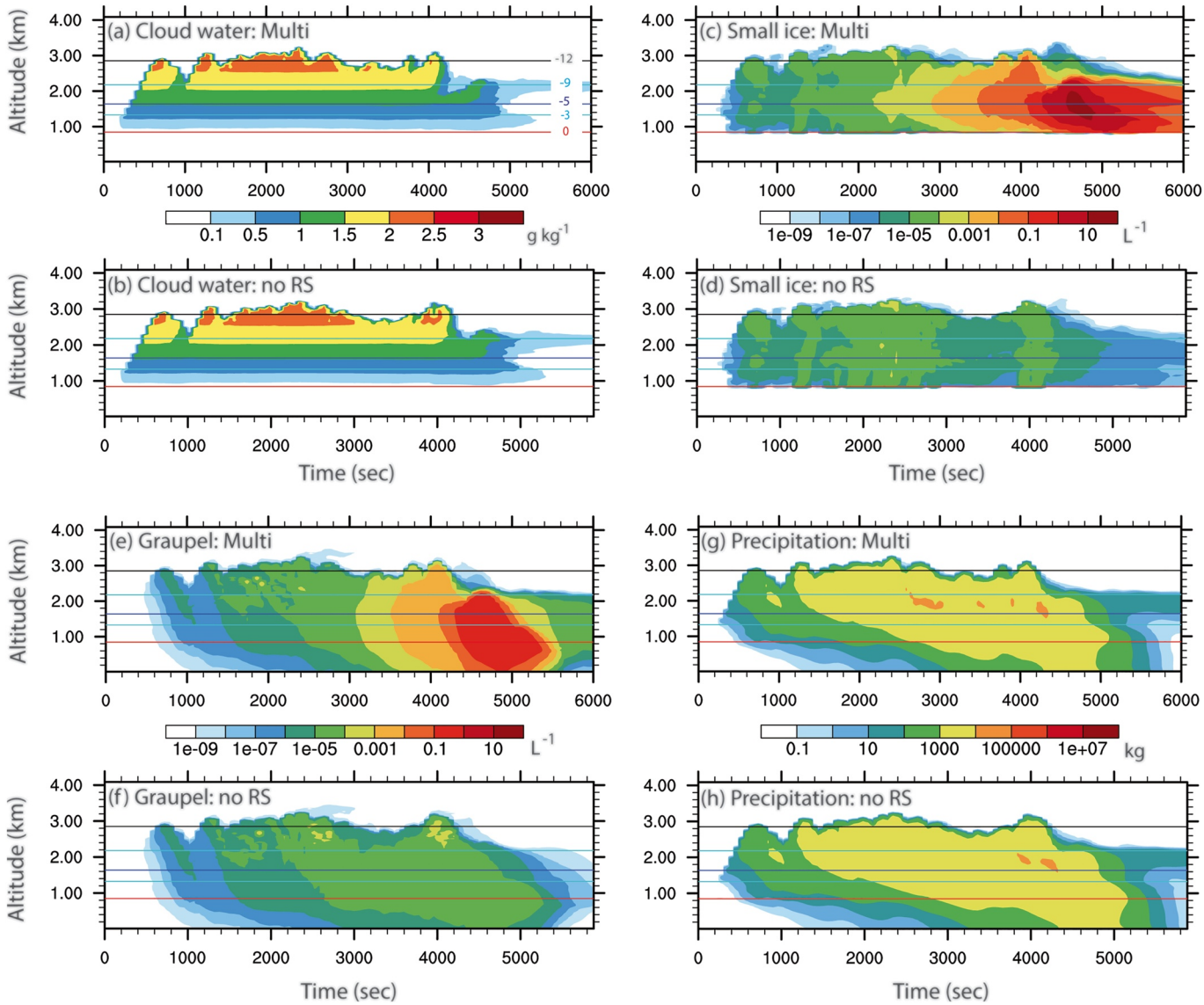

Figure 7. Pairs of time-height diagrams for the multi-updraft "Multi" simulation, and the same simulation but with rime splintering disabled "no RS." Panels show (a) and (b) Maximum cloud water mixing ratio; (c) and (d) Maximum small ice number concentration; (e) and (f) Maximum graupel (including frozen raindrops) number concentration, and (g) and (h) Total precipitation (rain, snow, and graupel) mass. Color bar in the middle of each pair denotes values used in shading. Horizontal lines denote isotherms in °C as labeled in panel (a), with the pair of aqua lines denoting the rime-splintering zone, with the dark blue line showing the peak production at −5°C.

splintering greatly increased the maximum ice number concentrations, its effect in the cloud upon precipitation was still minimal (Figures 7g and 7h).

Despite the high ice number concentrations produced in the simulation with rime splintering, and the feedback into additional graupel/frozen raindrop mass, the maximum frozen mass (also including snow and small ice) in the cloud only comprised 17% of the total cloud mass by the end of both simulations. The supercooled cloud drops and raindrops still greatly dominated the total hydrometeor mass in the cloud, in accord with satellite studies and other observational studies of clouds in the Southern Ocean, including those of SOCRATES.

Given the uncertainty of the true amount of INP active in the temperature range of the rime-splintering zone, additional multiple updraft simulations were conducted with different amounts of INP (Figure 8). The results were generally straightforward, at first. Initiating three orders of magnitude more INP in the model [more consistent with the extrapolated INP estimates of Vignon et al. (2021) at −5°C] decreased the time (and thus number of

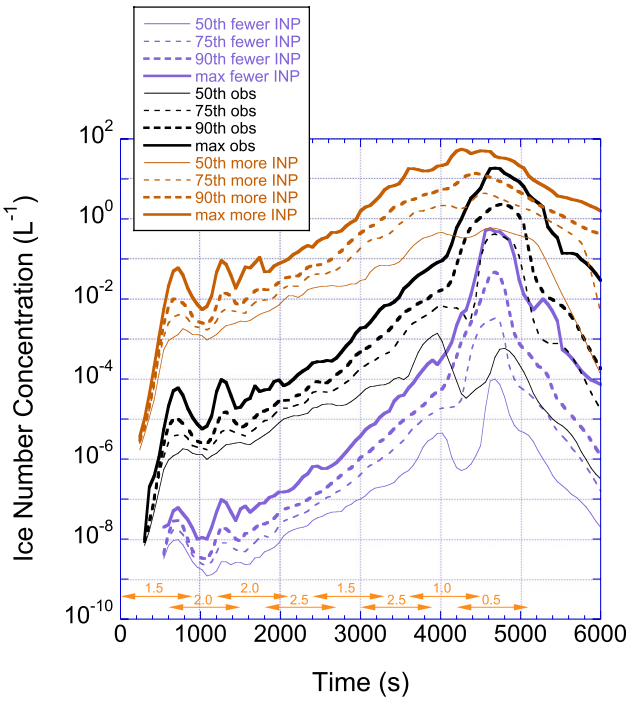

Figure 8. Time series of percentiles of small ice number concentration as labeled for the default multi-updraft simulation using INP based on the observed values (black), and for the same multi-updraft simulation but using a factor of 1000 fewer INP (purple) or a factor of 1000 more INP (brown). Orange arrows at bottom denote the time that the forcing for each updraft was applied as listed in Table 1, with the maximum strength in m s^{-2} labeled.

updrafts) required to attain ice number concentrations of 10 L^{-1}. Reducing the INP by three orders of magnitude failed to produce ice number concentrations more than 0.1 L^{-1}. Even the simulation using many more INP was still incapable of producing much larger amounts of ice within a single updraft. The low amounts of INP in this region appear to limit the effectiveness of rime splintering unless the cloud lifetimes can be extended through a number of successive updrafts. Interestingly, near the second half of the simulations, the percentiles of ice number concentration across the simulations differed less, and the maxima were all attained at nearly the same time, when the updraft forcing was weakening and no longer sufficient to support graupel/frozen raindrops so they fell through the rime-splintering zone. This result demonstrates the importance of cloud dynamics to rime splintering. The conversion of water mass to ice mass (not shown) did proceed faster in the simulation with a factor of 1000 more INP, however. The additional primary nucleated ice allowed more plentiful diffusional and/or riming growth to make more snow and graupel to also enable rime splintering, with 41% of the total cloud mass consisting of ice (at the time of the maximum graupel mass in the cloud) compared to the 17% simulated with the original INP amounts. Thus, although the simulations were not carried out to complete glaciation of the clouds, these results suggest that the speed of cloud glaciation, even when considering rime splintering, is highly dependent upon the amount of INP ingested by the cloud.

4. Conclusions and Discussion

This study sought to understand why numerous studies have indicated that the Southern Ocean shallow cumuli mainly consist of supercooled water, while others have sometimes observed large numbers of ice particles in the clouds that implicated a productive rime-splintering mechanism. This study is the first to use observations of INP acquired *in the same environment as the sampled Southern Ocean cumuli* to constrain primary nucleation of ice and its feedback into rime splintering in accompanying idealized, high-resolution numerical simulations. The main conclusions from this study are:

1. Of the 32 cloud passes through cumuli sampled at temperatures from −3 to −9°C, 62% had at least 1 L^{-1} ice detected by the PHIPS probe, or exhibited graupel/frozen raindrops in the 2DC images. Possible impacts of particle shattering on the PHIPS probe were carefully addressed.
2. These cloud passes were analyzed for evidence of rime splintering, using criteria requiring supercooled cloud droplets exceeding 25 μm diameter, 2DC images of graupel/rimed frozen raindrops, and ice between 20 to 60 μm diameter detected by the PHIPS probe exceeding 3.8 L^{-1}. Rime splintering was deemed *likely* in 34% (11) of these cloud passes, with an additional 9% (3) *possibly* having rime splintering but lacking definitive quantification of the small ice. Averaged ice number concentrations often ranged from tens to hundreds per liter, while the ice-nucleating particle (INP) measurements, extrapolated to the higher temperatures of the sampled clouds, were on the order of 10^{-6} L^{-1} or less.
3. All cloud passes that were deemed as *likely* or *possibly* having rime splintering had a multiple updraft structure and contained graupel/rimed frozen raindrops.
4. Numerical simulations based on the observed clouds, nucleating primary ice not only from extrapolations of the observed immersion-freezing INP but also including the effects of rime splintering, were unable to reproduce the high ice number concentrations observed if they only contained a single updraft, but created up to seven orders of magnitude more ice crystals when containing a sequence of multiple updrafts. The later updrafts enhanced liquid water for riming and re-introduced graupel/frozen raindrops into the rime-splintering zone for creation of additional ice.
5. Even in the multiple-updraft simulations where rime splintering created ice prolifically, the overall liquid mass still tended to dominate over the mass of ice in the clouds, but less so when the number of INP were greatly increased.

Thus, it appears that the prevalence of supercooled liquid clouds in Southern Ocean cumuli may result from (a) the paucity of INP in that region and (b) their inability to initiate significant rime splintering in the cloud without the assistance of multiple updrafts to extend cloud lifetimes and allow more larger frozen hydrometeors to form. The results indicate that if high numbers of INP, from parameterizations based on data in other locations, are assumed valid for regions with far fewer INP like the Southern Ocean, the speed of cloud glaciation (assisted by rime splintering) may be overestimated, which in turn would underestimate their reflection of solar radiation, as discussed and corroborated by past studies listed in the introduction. The suggestion of multiple updrafts enhancing the rime-splintering process over time in cumulus clouds has also been suggested in past studies (e.g., Blyth & Latham, 1993, 1997; Heymsfield & Willis, 2014; Lasher-Trapp et al., 2016; Mossop et al., 1970) and appears in this dataset to be a necessary factor for rime splintering to be effective; disregard of that dependency may also inflate glaciation rates (and thus underestimate solar radiation reflection) in this region. This study does not preclude the importance of other possible secondary ice production mechanisms such as the shattering of freezing raindrops (Lauber et al., 2018) that has been implicated in studies for other regions (e.g., Lawson et al., 2015). It seems reasonable that other time-dependent mechanisms of secondary ice production would also benefit from multi-updraft clouds for similar reasons.

Uncertainty in the results due to both observational and numerical modeling limitations motivates future work. The major limitations include:

1. The INP active at the temperatures of interest were too rare to be detected during the aerosol sampling period, so the observations had to be extrapolated to higher temperatures for numerical modeling. Interestingly, the succession of updrafts containing those rare INP was capable of producing enough ice to initiate rime splintering in the model. Perhaps no major, yet undiscovered source of INP active at higher temperatures is needed to explain the high numbers of ice sometimes observed.
2. Only two days during the SOCRATES field campaign were dedicated to sampling small cumuli. A larger number of cases in this region having different environmental thermodynamic conditions would test the generality of the results presented here.
3. The quantification and sizing of ice hydrometeors was still limited by the airborne microphysical probes. The PHIPS instrument was of great use in this study, but the small sampling volume required for single-particle analysis necessarily limits the representativeness of the data collected in small clouds, and particularly of the rarer hydrometeors. Those probes with larger sampling volumes like the 2DC are less conclusive in discriminating between smaller liquid and frozen hydrometeors.
4. The dynamical history of the sampled clouds was unknown. Thus, the minimum cloud top temperature of the sampled clouds is also unknown, as well as the realism of the dynamically forced updrafts, including their strength, placement and longevity in the simulated clouds. Documentation of the cloud dynamics and lifetime requires a ground-based radar, perhaps deployed on a small island (e.g., the Rain in Cumulus over the Ocean field campaign- Rauber et al., 2007). Having a time history that extended into the stage of cloud dissipation, along with in situ sampling by aircraft, would also help create a complete picture of the glaciation process. The mechanism(s) responsible for exciting multiple updrafts in oceanic clouds, and controls on their timing and characteristics, awaits further study.

Data Availability Statement

The NSF SOCRATES campaign data set is publicly available and can be accessed at https://data.eol.ucar.edu/master_lists/generated/socrates/. The CM1 model is freely available for download, and the model name lists, sounding, and alterations to the code for this study, are available through the Illinois Digital Environment for Access to Learning and Scholarship (IDEALS; http://hdl.handle.net/2142/111645), a digital depository library at the University of Illinois at Urbana-Champaign.

Acknowledgments
The unique SOCRATES data set was made possible by the campaign organizers and participants, and forecasting support by the Bureau of Meteorology. Processing of the aircraft data was performed by the Research Air Facility of the National Center for Atmospheric Research (NCAR; sponsored by the National Science Foundation), and simulations were run on the Cheyenne supercomputer provided by NCAR's Computational and Information Systems Laboratory. This study used the open-source CM1 model written and maintained by Dr. George Bryan of NCAR, and the NSSL microphysical parameterization written and maintained by Dr. Ted Mansell of the National Severe Storms Laboratory (funded by the National Oceanic and Atmospheric Administration); Dr. Mansell also provided some guidance for the implementation of the new immersion freezing algorithm.The participation of SLT and ES in SOCRATES and their analysis and modeling was supported by NSF grant AGS-1762096, the participation and data analysis of EJ, MS and FW was funded by DFG grant JA 2818/1-1, and of PD, CM and TH by NSF grant AGS-1660486. Ezra Levin is acknowledged for his role in readying instrumentation used for particle collection immersion freezing measurements using the CSU ice spectrometer, and Anne Marie Rauker for INP measurements. Dr. Greg McFarquhar and Dr. Robert Rauber provided useful discussions in the early stages of this work.

References

Abdelmonem, A., Jarvinen, E., Duft, D., Hirst, E., Vogt, S., Leisner, T., & Schnaiter, M. (2016). PHIPS-HALO: The airborne Particle Habit Imaging and Polar Scattering probe – Part 1: Design and operation. *Atmospheric Measurement Techniques*, *9*, 3131–3144. https://doi.org/10.5194/amt-9-3131-2016

Baumgardner, D., & Rodi, A. (1989). Laboratory and wind tunnel evaluations of the Rosemount Icing Detector. *Journal of Atmospheric and Oceanic Technology*, *6*(6), 971–979. https://doi.org/10.1175/1520-0426(1989)006<0971:lawteo>2.0.co;2

Bigg, E. K. (1953). The formation of atmospheric ice crystals by the freezing of droplets. *Quarterly Journal of the Royal Meteorological Society*, *79*(342), 510–519.

Blyth, A. M., & Latham, J. (1993). Development of ice and precipitation in New Mexican summertime cumulus clouds. *Quarterly Journal of the Royal Meteorological Society*, *119*, 91–120. https://doi.org/10.1002/qj.49711950905

Blyth, A. M., & Latham, J. (1997). A multi-thermal model of cumulus glaciation via the Hallett-Mossop process. *Quarterly Journal of the Royal Meteorological Society*, *123*(541), 1185–1198. https://doi.org/10.1002/qj.49712354104

Bodas-Salcedo, A., Hill, P. G., Furtado, K., Williams, K. D., Field, P. R., Manners, J. C., et al. (2016). Large contribution of supercooled liquid clouds to the solar radiation budget of the Southern Ocean. *Journal of Climate*, *29*(11), 4213–4228. https://doi.org/10.1175/JCLI-D-15-0564.1

Bodas-Salcedo, A., Williams, K. D., Ringer, M. A., Beau, I., Cole, J. N. S., Dufresne, J.-L., et al. (2014). Origins of the solar radiation biases over the Southern Ocean in CFMIP2 models*. *Journal of Climate, 27*(1), 41–56. https://doi.org/10.1175/jcli-d-13-00169.1

Bohm, H. P. (1989). A general equation for the terminal fall speed of solid hydrometeors. *Journal of the Atmospheric Sciences*, *46*(15), 2419–2427. https://doi.org/10.1175/1520-0469(1989)046<2419:agefft>2.0.co;2

Bryan, G. H., & Fritsch, J. M. (2002). A benchmark simulation for Moist Nonhydrostatic Numerical Models. *Monthly Weather Review*, *130*(12), 2917–2928. https://doi.org/10.1175/1520-0493(2002)130<2917:absfmn>2.0.co;2

Bunker, K. W., China, S., Mazzoleni, C., Kostinski, A., & Cantrell, W. (2012). Measurements of ice nucleation by mineral dusts in the contact mode. *Atmospheric Chemistry and Physics Discussions*, *12*(8), 20291–20309. https://doi.org/10.5194/acpd-12-20291-2012

Choularton, T. W., Latham, J., & Mason, B. J. (1978). A possible mechanism of ice splinter production during riming. *Nature*, *274*(5673), 791–792. https://doi.org/10.1038/274791a0

Cotton, W. R., Tripoli, G. J., Rauber, R. M., & Mulvihill, E. A. (1986). Numerical simulation of the effects of varying ice crystal nucleation rates and aggregation processes on orographic snowfall. *Journal of Climate and Applied Meteorology*, *25*(11), 1658–1680. https://doi.org/10.1175/1520-0450(1986)025<1658:NSOTEO>2.0.CO;2

D'Alessandro, J. J., McFarquhar, G. M., Wu, W., Stith, J. L., Jensen, J. B., & Rauber, R. M. (2021). Characterizing the occurrence and spatial heterogeneity of liquid, ice and mixed phase low-level clouds over the Southern Ocean using in situ observations acquired during SOCRATES. *Journal of Geophysical Research: Atmospheres, 126*, e2020JD034482. https://doi.org/10.1029/2020JD034482

DeMott, P. J., Hill, T. C. J., McCluskey, C. S., Prather, K. A., Collins, D. B., Sullivan, R. C., et al. (2016). Sea spray aerosol as a unique source of ice nucleating particles. *Proceedings of the National Academy of Sciences*, *113* (21), 5797–5803. https://doi.org/10.1073/pnas.1514034112

Field, P. R., Lawson, R. P., Brown, P. R. A., Lloyd, G., Westbrook, C., Moisseev, D., et al. (2017). Chapter 7. Secondary ice production - Current state of the science and recommendations for the future. *Meteorological Monographs*. https://doi.org/10.1175/amsmonographs-d-16-0014.1

Finlon, J. A., Rauber, R. M., Wu, W., Zaremba, T. J., McFarquhar, G. M., Nesbitt, S. W., et al. (2020). Structure of an atmospheric river over Australia and the Southern Ocean: II. Microphysical evolution. *Journal of Geophysical Research: Atmospheres*, *125*, e2020JD032514. https://doi.org/10.1029/2020JD032514

Frey, W. R., & Kay, J. E. (2018). The influence of extratropical cloud phase and amount feedbacks on climate sensitivity. *Climate Dynamics*, *50*(7-8), 3097–3116. https://doi.org/10.1007/s00382-017-3796-5

Hallett, J., & Mossop, S. C. (1974). Production of secondary ice particles during the riming process. *Nature*, *249*(5452), 26–28. https://doi.org/10.1038/249026a0

Hallett, J., Sax, R. I., Lamb, D., & Murty, A. S. R. (1978). Aircraft measurements of ice in Florida cumuli. *Quarterly Journal of the Royal Meteorological Society*, *104*, 631–651. https://doi.org/10.1002/qj.49710444108

Halverson, J. B., Simpson, J., Heymsfield, G., Pierce, H., Hock, T., & Ritchie, L. (2006). Warm core structure of Hurricane Erin diagnosed from high altitude dropsondes during CAMEX-4. *Journal of the Atmospheric Sciences*, *63*(1), 309–324. https://doi.org/10.1175/JAS3596.1

Heymsfield, A., & Willis, P. (2014). Cloud conditions favoring secondary ice particle production in tropical maritime convection. *Journal of the Atmospheric Sciences*, *71*(12), 4500–4526. https://doi.org/10.1175/JAS-D-14-0093.1

Hock, T. F., & Franklin, J. L. (1999). The NCAR GPS Dropwindsonde. *Bulletin of the American Meteorological Society*, *80*(3), 407–420. https://doi.org/10.1175/1520-0477(1999)080<0407:tngd>2.0.co;2

Hu, Y., Rodier, S., Xu, K.-M., Sun, W., Huang, J., Lion, B., et al. (2010). Occurrence, liquid water content, and fraction of supercooled water clouds from combined CAKIOP/IIR/MODIS measurements. *Journal of Geophysical Research: Atmospheres*, *115*, D00H34. https://doi.org/10.1029/2009JD012384

Huang, S., Hu, W., Chen, J., Wu, Z., Zhang, D. & Fu, P. (2021). Overview of biological ice nucleating particles in the atmosphere. *Environment International*, *146*, 106197. https://doi.org/10.1016/j.envint.2020.106197

Huang, Y., Chubb, T., Baumgardner, D., deHoog, M., Siems, S. T., & Manton, M. J. (2017). Evidence for secondary ice production in Southern Ocean open cellular convection. *Quarterly Journal of the Royal Meteorological Society*, *143*(704), 1685–1703. https://doi.org/10.1002/qj.3041

Huang, Y., Siems, S. T., & Manton, M. J. (2021). Wintertime in-situ cloud microphysical properties of mixed-phase clouds over the Southern Ocean. *Journal of Geophysical Research: Atmospheres*, *126*, e2021JD034832. https://doi.org/10.1029/2021JD034832

Huang, Y., Siems, S. T., Manton, M. J., Protat, A., & Delanoë, J. (2012). A study on the low-altitude clouds over the Southern Ocean using the DARDAR-MASK. *Journal of Geophysical Research: Atmospheres*, *117*(D18). https://doi.org/10.1029/2012JD017800

Kay, J. E., Medeiros, B., Hwang, Y.-T., Gettelman, A., Perket, J., & Flanner, M. G. (2014). Processes controlling Southern Ocean shortwave climate feedbacks in CESM. *Geophysical Research Letters*, *41*(2), 616–622. https://doi.org/10.1002/2013GL058315

Korolev, A. V., Emery, E. F., Strapp, J. W., Cober, S. G., Isaac, G. A., Wasey, M., & Marcotte, D. (2011). Small ice particles in tropospheric clouds: Fact or artifact? Airborne icing instrumentation evaluation experiment. *Bulletin of the American Meteorological Society*, *92*, 967–973. https://doi.org/10.1175/2010BAMS3141.1

Kremser, S., Harvey, M., Kuma, P., Hartery, S., Saint-Macary, A., McGregor, J., et al. (2021). Southern Ocean cloud and aerosol data: A compilation of measurements from the 2018 Southern Ocean Ross Sea Marine Ecosystems and Environment voyage. *Earth System Science Data*, *13*(7), 3115–3153. https://doi.org/10.5194/essd-13-3115-2021

Lance, S., Brock, C. A., Rogers, D., & Gordon, J. A. (2010). Water droplet calibration of the Cloud Droplet Probe (CDP) and in-flight performance in liquid, ice and mixed-phase clouds during ARCPAC. *Atmospheric Measurement Techniques*, *3*(6), 1683–1706. https://doi.org/10.5194/amt-3-1683-2010

Lasher-Trapp, S., Leon, D. C., DeMott, P. J., Villanueva-Birriel, C. M., Johnson, A. V., Moser, D. H., et al. (2016). A multisensor investigation of rime splintering in tropical maritime cumuli. *Journal of the Atmospheric Sciences*, *73*(6), 2547–2564. https://doi.org/10.1175/JAS-D-15-0285.1

Lauber, A., Kiselev, A., Pander, T., Handmann, P., & Leisner, T. (2018). Secondary ice formation during freezing of levitated droplets. *Journal of the Atmospheric Sciences*, *75*, 28152826. https://doi.org/10.1175/JAS-D-18-0052.1

Lawson, R. P., O'Connor, D., Zmarzly, P., Weaver, K., Baker, B., Mo, Q., & Jonsson, H. (2006). The 2D-S (Stereo) probe: Design and preliminary tests of a new airborne, high-speed, high-resolution particle imaging probe. *Journal of Atmospheric and Oceanic Technology*, *23*(11), 1462–1477. https://doi.org/10.1175/JTECH1927.1

Lawson, R. P., Woods, S., & Morrison, H. (2015). The microphysics of ice and precipitation development in tropical cumulus clouds. *Journal of the Atmospheric Sciences*, *72*, 2429–2445. https://doi.org/10.1175/JAS-D-14-0274.1

Levin, E. J. T., DeMott, P. J., Suski, K. J., Boose, Y., Hill, T. C. J., McCluskey, C. S., et al. (2019). Characteristics of ice nucleating particles in and around California winter storms. *Journal of Geophysical Research: Atmospheres*, *124*(21), 11530–11551. https://doi.org/10.1029/2019JD030831

Lew, J. K., & Pruppacher, H. R. (1983). A theoretical determination of the capture efficiency of small columnar ice crystals by large cloud drops. *Journal of the Atmospheric Sciences*, *40*(1), 139–145. https://doi.org/10.1175/1520-0469(1983)040<0139:ATDOTC>2.0.CO;2

Mace, G. G., Benson, S., & Hu, Y. (2020). On the frequency of occurrence of the ice phase in supercooled Southern Ocean low clouds derived from CALIPSO and CloudSat. *Geophysical Research Letters*, *47*, e2020GL087554. https://doi.org/10.1029/2020GL087554

Mansell, E. R., Ziegler, C. L., & Bruning, E. C. (2010). Simulated electrification of a small thunderstorm with two-moment bulk microphysics. *Journal of the Atmospheric Sciences*, *67*(1), 171–194. https://doi.org/10.1175/2009JAS2965.1

McCluskey, C. S., Hill, T. C. J., Humphries, R. S., Rauker, A. M., Moreau, S., Strutton, P. G., et al. (2018). Observations of ice nucleating particles over Southern Ocean waters. *Geophysical Research Letters*, *45*(11). https://doi.org/10.1029/2018GL079981

McCoy, D. T., Hartmann, D. L., & Grosvenor, D. P. (2014). Observed Southern Ocean cloud properties and shortwave reflection. Part II: Phase changes and low cloud feedback*. *Journal of Climate*, *27*(23), 8858–8868. https://doi.org/10.1175/JCLI-D-14-00288.1

McFarquhar, G. M., Bretherton, C. S., Marchand, R., Protat, A., DeMott, P. J., Alexander, S. P., et al. (2021). Observations of clouds, aerosols, precipitation, and surface radiation over the Southern Ocean: An overview of CAPRICORN, MARCUS, MICRE, and SOCRATES. *Bulletin of the American Meteorological Society*, *102*(4), E894–E928. https://doi.org/10.1175/BAMS-D-20-0132.1

Meyers, M. P., DeMott, P. J., & Cotton, W. R. (1992). New primary ice-nucleation parameterizations in an explicit cloud model. *Journal of Applied Meteorology*, *31*(7), 708–721. https://doi.org/10.1175/1520-0450(1992)031<0708:NPINPI>2.0.CO;2

Moser, D. H., & Lasher-Trapp, S. (2017). The influence of successive thermals on entrainment and dilution in a simulated cumulus congestus. *Journal of the Atmospheric Sciences*, *74*(2), 375–392. https://doi.org/10.1175/JAS-D-16-0144.1

Mossop, S. C. (1976). Production of secondary ice particles during the growth of graupel by riming. *Quarterly Journal of the Royal Meteorological Society*, *102*(431), 45–57. https://doi.org/10.1002/qj.49710243104

Mossop, S. C. (1980). The mechanism of ice splinter production during riming. *Geophysical Research Letters*, *7*(2), 167–169. https://doi.org/10.1029/GL007i002p00167

Mossop, S. C., Ono, A., & Wishart, E. R. (1970). Ice particles in maritime clouds near Tasmania. *Quarterly Journal of the Royal Meteorological Society*, *96*(409), 487–508. https://doi.org/10.1002/qj.49709640910

Naud, C. M., Booth, J. F., & Del Genio, A. D. (2014). Evaluation of ERA-Interim and MERRA cloudiness in the Southern Ocean. *Journal of Climate*, *27*(5), 2109–2124. https://doi.org/10.1175/jcli-d-13-00432.1

O'Shea, S. J., Choularton, T. W., Flynn, M., Bower, K. N., Gallagher, M., Crosier, J., et al. (2017). In situ measurements of cloud microphysics and aerosol over coastal Antarctica during the MAC campaign. *Atmospheric Chemistry and Physics*, *17*(21), 13049–13070. https://doi.org/10.5194/acp-17-13049-2017

Pinto, J. O. (1998). Autumnal mixed-phase cloudy boundary layers in the Arctic. *Journal of the Atmospheric Sciences*, *55*(11), 2016–2038. https://doi.org/10.1175/1520-0469(1998)055<2016:ampcbl>2.0.co;2

Rangno, A. L., & Hobbs, P. V. (1983). Production of ice particles in clouds due to aircraft penetrations. *Journal of Climate and Applied Meteorology*, *22*(2), 214–232. https://doi.org/10.1175/1520-0450(1983)022<0214:POIPIC>2.0.CO;2

Rauber, R. M., Stevens, B., Ochs, H. T., Knight, C., Albrecht, B. A., & Blyth, A. M. et al. (2007). Rain in shallow cumulus over the ocean: The RICO Campaign. *Bulletin of the American Meteorological Society*, *88*(12), 1912–1928. https://doi.org/10.1175/BAMS-88-12-1912

Saliba, G., Sanchez, K. J., Russell, L. M., Twohy, C. H., Roberts, G. C., Lewis, S., et al. (2021). Organic composition of three different size ranges of aerosol particles over the Southern Ocean. *Aerosol Science and Technology*, *55*(3), 268–288. https://doi.org/10.1080/02786826.2020.1845296

Schnaiter, M., Järvinen, E., Abdelmonem, A., & Leisner, T. (2018). PHIPS-HALO: The airborne particle habit imaging and polar scattering probe – Part 2: Characterization and first results. *Atmospheric Measurement Techniques*, *11*(1), 341–357. https://doi.org/10.5194/amt-11-341-2018

Trenberth, K. E., & Fasullo, J. T. (2010). Simulation of present-day and twenty-first-century energy budgets of the southern oceans. *Journal of Climate*, *23*(2), 440–454. https://doi.org/10.1175/2009JCLI3152.1

Vergara-Temprado, J., Miltenberger, A. K., Furtado, K., Grosvenor, D. P., Shipway, B. J., Hill, A. A., et al. (2018). Strong control of Southern Ocean cloud reflectivity by ice-nucleating particles. *Proceedings of the National Academy of Sciences*, *115* (11) 2687–2692. https://doi.org/10.1073/pnas.1721627115

Vignon, É., Alexander, S. P., DeMott, P. J., Sotiropoulou, G., Gerber, F., Hill, T. C. J., et al., (2021). Challenging and improving the simulation of mid-level mixed-phase clouds over the high- latitude Southern Ocean. *Journal of Geophysical Research: Atmospheres*, *126*, e2020JD033490. https://doi.org/10.1029/2020jd033490

Vivekanandan, J., Ellis, S., Tsai, P., Loew, E., Lee, W.-C., Emmett, J., et al. (2015). A wing pod-based millimeter wavelength airborne cloud radar. *Geoscientific Instrumentation, Methods and Data Systems*, *4*(2), 161–176. https://doi.org/10.5194/gi-4-161-2015

Waitz, F., Schnaiter, M., Leisner, T., & Järvinen, E. (2021). PHIPS-HALO: The airborne Particle Habit Imaging and Polar Scattering probe – Part 3: Single-particle phase discrimination and particle size distribution based on the angular-scattering function, *Atmospheric Measurement Techniques*, *14*(4), 3049–3070. https://doi.org/10.5194/amt-14-3049-2021

Williams, K. D., Bodas-Salcedo, A., Déqué, M., Fermepin, S., Medeiros, B., Watanabe, M., et al. (2013). The transpose-AMIP II experiment and its application to the understanding of Southern Ocean cloud biases in climate models. *Journal of Climate*, *26*(10), 3258–3274. https://doi.org/10.1175/jcli-d-12-00429.1

Zaremba, T. J., Rauber, R. M., McFarquhar, G. M., Hayman, M., Finlon, J. A., & Stechman, D. M. (2020). Phase characterization of cold sector Southern Ocean cloud tops: Results from SOCRATES. *Journal of Geophysical Research: Atmospheres*, *125*, e2020JD033673. https://doi.org/10.1029/2020JD033673